2026 IEEE International Conference on Robotics and Automation (ICRA 2026)
June 1-5, 2026. Vienna, Austria

Development of a Miniaturized 6-DoF Surgical Instrument with a 4-mm Elbow and 3-mm Wrist for Transoral Robotic Surgery

Catie Balasubramanian[1], Sunny Zhang[1], Teng Li[1], Paul H. Kang[1], Ali A. Nazari[1], Thomas Looi[1,2], and Dale J. Podolsky[1,2,3]

dale.podolsky@sickkids.ca

***Abstract*— Current platforms for Transoral Robotic Surgery (TORS) are suboptimal for confined oropharyngeal workspaces, particularly in pediatric applications. To address this, we present the design and characterization of a novel cable-driven robotic instrument providing 6 degrees-of-freedom (DoF)—shaft roll, elbow pitch/yaw, wrist pitch/yaw, and grip—for dexterous manipulation. The system integrates a miniaturized 4-mm proximal elbow with a previously developed 3-mm distal wrist. This architecture is enabled by a novel "sandwich" link architecture that facilitates high-density cable routing through the joint's center plane, providing a compact, rigid alternative to traditional pin-jointed designs. Experimental validation identified significant kinematic coupling between in-plane joint pairs. An empirical real-time compensation strategy reduced this coupling rate by 82.9% for pitch and 80.8% for yaw. Workspace analysis confirmed the proximal elbow enables high distal dexterity at regions critical for complex surgical tasks. Integration with a Franka Research 3 manipulator enabled fully coordinated macro-micro teleoperation, providing a pilot demonstration for TORS workflows. This represents the first demonstration of a 4-mm elbow-3mm wrist mechanism for TORS, providing the hardware foundation necessary for future evaluation of dexterity-intensive tasks, including suturing and dissection.**

I. Introduction

A. Background

TORS provides improved access to the oropharyngeal cavity, resulting in improved patient outcomes [1], [2]. However, the most widely adopted clinical robotic platforms were originally designed for large-cavity procedures rather than the specific anatomical constraints of TORS. While some robotic platforms, such as the Senhance system (Asensus Surgical, Durham, NC, USA), offer 3-mm instruments suitable for pediatric use, these tools are rigid and lack distal articulation. Krebs et al. demonstrated the feasibility of Senhance-based robotic infant surgery using these 3-mm instruments, but noted that the absence of wristed articulation limits dexterity, explicitly calling for the development of 3-mm wristed instruments to improve outcomes in pediatric procedures [3]. Consequently, clinical practice often relies on repurposed general-surgery platforms, creating tool–anatomy mismatch and challenges operating within more confined spaces [4], [5]. These constraints are particularly pronounced in infants and young children, where dexterity-dependent tasks such as suturing or delicate dissection are hindered by instrument collisions, limited reach, and restricted visualization. As a result, compromises in tool orientation, line-of-sight, and maneuverability can negatively impact surgical performance and outcomes.

B. Transoral Robotic Surgery (TORS)

The da Vinci® Xi and 5 systems (Intuitive Surgical Inc., Sunnyvale, CA, USA) represent the most widely used platforms for TORS, having seen widespread adoption and clinical success in adult hospitals [6], [7]. However, when applied to more confined workspaces, their 8-mm EndoWrist® instruments [8], [9], having originally been designed for large body cavity procedures, can be difficult to articulate. During TORS, two arms must triangulate through the oral aperture alongside an endoscope, which can result in significant tool-tool and tool-cavity collisions. These collisions present serious clinical risks, including unintended tissue trauma (e.g., pharyngeal lacerations or dental injury), unpredictable loss of distal precision, and disruption of the endoscopic visual field, all of which severely limit the safe performance of complex surgical tasks.

Single-port systems, such as the da Vinci SP [10] or the Vicarious Surgical Robotic System (Vicarious Surgical Inc., Waltham, MA, USA), reduce triangulation-related collisions by incorporating a proximal "elbow" joint that allows the instruments and endoscope to traverse through a single trocar and deploy within a cavity [11]. However, for TORS, the instruments remain too large with a suboptimal elbow position, which can limit performance within confined spaces. In addition, these systems were designed for single-incision procedures rather than oral access [11], [12].

Thus, there is a clear need for a TORS-specific instrument that achieves multi-DoF distal articulation within a miniaturized profile compatible with the confined pediatric oropharyngeal workspace, without the size and access constraints of existing multi-port or single-port platforms.

C. Prior Work

Our group previously developed a 3-mm diameter cable-driven, pin-jointed wrist that integrates with the da Vinci

[1] C. Balasubramanian, S. Zhang, T. Li, P. Kang, A. Nazari, T. Looi, and D. Podolsky are with the Wilfred and Joyce Posluns Centre for Image Guided Innovation & Therapeutic Intervention (PCIGITI), Hospital for Sick Children (SickKids), Toronto, Canada.

[2] T. Looi and D. Podolsky are with the Department of Mechanical and Industrial Engineering (MIE), University of Toronto, Toronto, Canada.

[3] D. Podolsky is with the Division of Plastic, Reconstructive and Aesthetic Surgery, Department of Surgery, University of Toronto, Toronto, Canada.

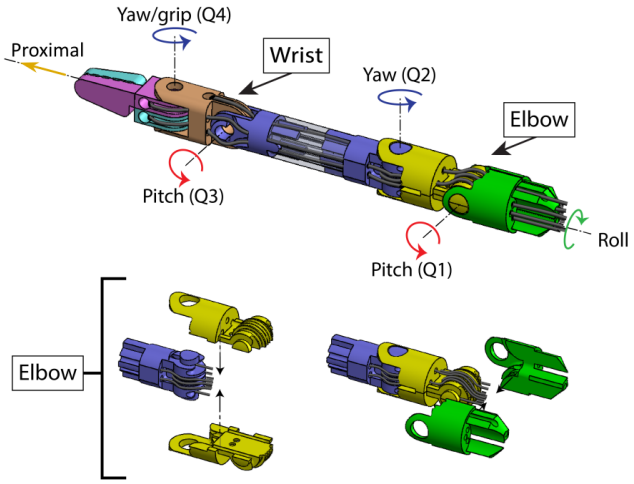

Fig. 1. Schematic of the elbow-wrist surgical instrument illustrating the elbow and wrist links with axis for each respective degree-of-freedom. Exploded view of the elbow mechanism with the sandwich design that eliminates the need for pins and allows for routing of tendons (cables) for elbow and wrist motion.

Research Kit (dVRK) for cleft palate surgery [13], [14]. The design employs cable guide channels that aid miniaturization and a proximal cam mechanism to decouple wrist pitch and yaw/grip [15]. This instrument outperformed 8-mm tools on a cleft palate simulator, demonstrating fewer collisions and improved visualization during suturing. Despite their compact size, bulk from the dVRK manipulators causes collisions that limit reachability, particularly near the posterior oropharyngeal cavity. We similarly evaluated the da Vinci SP (unpublished data); while its single-port architecture offered coordinated RCM orientation, the instruments remain too large for TORS. This work builds on these findings to develop a novel TORS architecture.

D. Contribution

This paper presents the design and characterization of a novel cable-driven elbow-wrist instrument for TORS, integrating a 2-DoF proximal elbow with our previously developed 3-mm distal wrist to provide 6 DoF (shaft roll; elbow pitch and yaw; wrist pitch and yaw; and wrist grip) at the smallest reported diameter for an elbow-wrist tool (Fig. 1). The contributions of this work are:

1) A novel ”sandwich” link architecture for miniaturized robotic joints that enables high-density cable routing (eight discrete tendons) within a 4-mm profile. By eliminating the central joint pin, this design provides unobstructed access to the joint’s centerplane—utilizing volume that is traditionally inaccessible—to facilitate collision-free tendon routing while maintaining high structural rigidity through a nested, fastener-free assembly.
2) The implementation of a multi-layer empirical kinematic control strategy that compensates for the complex mechanical coupling inherent in high-density guide-channel routing, achieving an over 80% reduction in unintended joint motion to enable decoupled motion control.

II. Tool Design

A. Design Goals and System Overview

The instrument is designed to provide a 3-mm distal wrist and 4-mm proximal elbow, each with 2-DoF revolute joints, separated by a minimal distance and coupled to a robotic manipulator for proximal roll and translation. The resulting system is 6-DoF with a PRRRRR configuration, comprising a prismatic insertion axis followed by five revolute joints (shaft roll, elbow pitch, elbow yaw, wrist pitch, and wrist yaw) with the addition of a grip function.

B. Elbow Mechanism

Miniaturizing a tendon-driven elbow requires routing of eight tendons through two proximal revolute joints while (i) isolating antagonistic pairs, (ii) respecting the minimum bending radius of the cable, and (iii) limiting path-length changes to minimize coupling. Our initial motivation for a novel mechanism stemmed from the spatial limits of our previous 3-mm wrist, which routed four tendons along the outer edges of a central pin. Scaling that traditional pin-joint approach to route eight tendons would have doubled the link diameter. To maintain miniaturization, we introduce a novel two-piece “sandwich” link architecture (Fig. 1), where the two proximal links are split. This creates a completely pin-less assembly in which rotation occurs about a bushing machined into the link halves. Fundamentally differing from previous pin-jointed designs, eliminating the central pin provides unobstructed access to the center plane of the joint. This internal clearance allows guide channels to be machined directly through the rotational axis—utilizing the volume traditionally occupied by a pin—enabling the routing of all eight distinct tendons through the miniaturized 4-mm space. Structural rigidity of the assembly is maintained through a nested mechanical interlocking design: the bushings of the distal link sandwich and secure the two halves of the proximal link, with the bottom-most link press-fit into the instrument shaft, enabling high rigidity during operation while permitting non-destructive disassembly for maintenance. Links were machined from stainless steel (3E Rapid Prototyping, Hong Kong). Machining constraints impose a 0.5-mm minimum through-hole, which in turn sets the feasible tendon size; we utilized 0.24-mm diameter, 7-strand braided tungsten cable (Carl Stahl Sava Industries Inc., Riverdale, NJ, USA) across the elbow and wrist joints to maximize strength and joint rotation without increasing link diameter. Surface finish and tolerances of the channel geometry were controlled to reduce friction compared with miniaturized guide-channel we have previously implemented [13], [14], [16].

Circular and spiral channels are used for cable routing. The circular channels are used to offset cables about an axis when geometry prohibits centerline routing, while spiral channels are used when geometry allows routing through (or

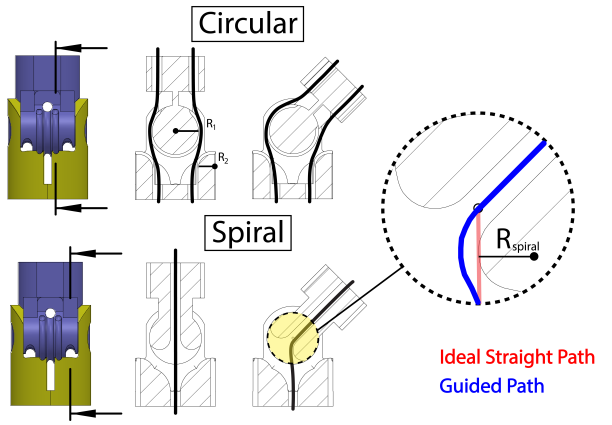

Fig. 2. Elbow joint cable routing illustrating its circular and spiral grooves. The cable routing (black lines) are illustrated for each groove type. The ideal versus guided path of the cable is illustrated for the spiral groove.

very near) the rotational axis. Spiral channels respect cable bend limits while minimizing path-length variation (Fig. 2).

The spiral channel radius is parameterized to satisfy the tendon's minimum bend, with the centerline radius given by:

$$r_{spiral} = 0.75 \sin\left(\frac{\theta}{2}\right), \qquad -\frac{\pi}{2} \leq \theta \leq \frac{\pi}{2}. \tag{1}$$

where θ is the joint angle. This choice minimizes cable path-length change, inducing a maximum change of 0.174 mm on the dependent cable when the independent joint is actuated 180°. Where circular channels are required, a compensation strategy must be used to enable decoupled joint control. Cross-sections of the elbow yaw joint illustrate both channel types and their allocation to the distal wrist joints (Fig. 2).

C. Wrist and End-Effector

The distal 3-mm wrist, previously described in [13], [14], provides 2 DoF (pitch, yaw/grip). It consists of four links featuring minimized cable guide channels for compact articulation, routing the same 0.24-mm braided tungsten tendons for pitch, yaw, and grip functions. On the transmission side, the original 3-mm tool utilized a proximal cam mechanism to mechanically decouple wrist pitch from yaw/grip. However, scaling this mechanical decoupling to support the increased complexity of the combined elbow-wrist system was unfeasible. Instead, the new tool's transmission fundamentally shifts to a software-based approach: antagonistic tendons for each DoF are driven by separate, independent actuators, relying entirely on the empirical algorithmic compensation strategy (detailed in Section III.D) to decouple the joints in real time.

D. Elbow-wrist Distance

The distance between the elbow and wrist in the initial prototype was determined by the spatial constraints of the infant oral cavity, as evaluated using the high-fidelity cleft palate simulator. A 2.2-cm separation was selected, permitting full elbow and wrist articulation within the infant oral cavity. This parameter, however, is adaptable and can be lengthened or shortened depending on the requirements of specific applications, with a minimum axis-axis distance of 12 mm.

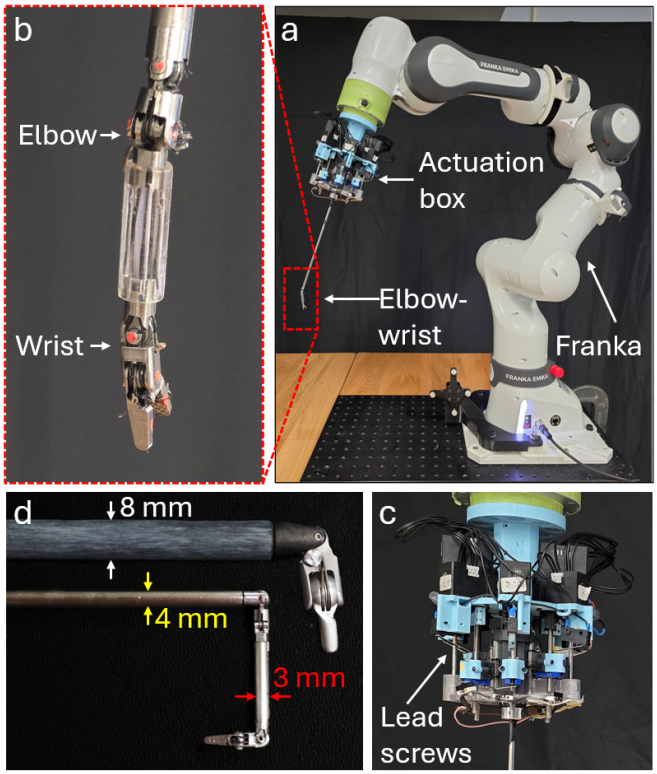

Fig. 3. a) Novel tool coupled to a Franka Research 3, illustrating the actuation box and tendon-driven elbow-wrist mechanism. b) Close-up visualization of the elbow and wrist mechanism. c) Close-up visualization of the actuation mechanism highlighting the lead screws for wrist motion, d) Size and manipulability comparison between existing 8-mm da Vinci instruments and the novel 3-mm elbow-wrist tool.

E. Actuation and System Integration

An actuation box using Dynamixel (ROBOTIS Co. Ltd, Seoul, South Korea) actuators tension and move the tendons. Elbow joint tendons are driven by capstans. Wrist joint tendons are driven by lead screws to enable independent antagonistic pre-tensioning and closed-loop differential control, which is necessary to compensate for tensile coupling. For benchtop evaluation, the tool was mounted on a Franka Research 3 (Franka Robotics, Munich, Germany) robotic arm, which provides precise positioning and tool-shaft roll and translation (Fig. 3). Coordinate conventions are fixed so that base-frame roll is clockwise as viewed from the robot base, which is illustrated in Fig. 1. A transparent wrist-elbow connector was 3D printed in Clear V5 resin on a Form4B printer (Formlabs, Inc., Somerville, MA, USA) which was used for testing. The clear connector enabled visualization of wrist actuation cables to support system assembly and repair during testing (Fig. 3b).

III. Joint Kinematic Modeling and Control

The forward joint kinematics of the elbow-wrist instrument involves investigating the cable routing and the motor-to-joint space kinematics. This section describes the two forms of mechanical coupling, the guide channel path length, the cable routing geometry, and the motor-to-joint space kinematics, where we present a coupling compensation strategy to achieve decoupled joint control.

A. Mechanical Coupling Analysis

As with the original 3-mm tool, the use of guide channels for cable routing introduces mechanical coupling, where motion at a proximal (upstream) joint unintentionally affects more distal (downstream) joints. The addition of redundant elbow joints into the design increases the number of coupled joint interactions, which must be accurately analyzed and compensated to enable precise robot end-effector control. We categorize these interactions into kinematic and tensile coupling on the basis of their effect on a downstream joint's antagonistic cable pair.

Kinematic coupling induces unintended motion when an upstream joint's rotation differentially changes a downstream joint's antagonistic cable lengths. This occurs for in-plane joint pairs routed on opposite sides of the rotational axis: Q1-Q3 (elbow-wrist pitch) and Q2-Q4 (elbow-wrist yaw).

Tensile coupling, the type of interaction originally analyzed in the 3-mm tool [13], affects cable tension. It occurs when the change in cable length of an antagonistic pair is symmetrical. This is a result of routing both cables through symmetrical channels on the same side of the axis of rotation, resulting in identical cable path length change as the joint actuates as shown in Fig. 1. This type of coupling occurs for the other joint pairs of the elbow-wrist mechanism (Q1-Q2, Q1-Q4, Q2-Q3, and Q3-Q4).

To compensate for these coupling effects, identifying and quantifying the dependencies of each downstream link is required. While the circular guide channels from previous work induce substantial deviations, the use of spiral guide channels for adjacent links (Q1-Q2 and Q2-Q3), enabled by the pinless design, avoids the same effect. The spiral guide channels induce a theoretical maximum path-length change of only 0.174mm on a cable passing through a joint articulated through the full 180-degree range of motion, as measured from path geometry in SolidWorks® 2022 (Dassault Systèmes, Vélizy-Villacoublay, France). This minor effect was considered negligible for the initial mechanism validation, as the path length change is symmetric across the antagonistic cable pair and therefore does not directly introduce positional error. Moreover, its magnitude is insignificant, accounting for less than 0.05% of the total cable length in this miniaturized driver setup. Therefore, the tensile coupling effects induced by the spiral channels were omitted from the compensation model.

Prior work has identified that, unlike the negligible effects from spiral guide channels, the coupling induced by the circular guide channels is significant and requires compensation. While the previous 3-mm wrist design employed a mechanical solution using spiral cams for decoupling wrist pitch and wrist yaw/grip, the increased number of coupled joints in our tool makes a software-based approach more practical.

To define this model, we establish the elbow-wrist tool in its straight configuration as the zero starting position, from which all joints are commanded to move in positive or negative directions. Since all joints are symmetrical about the plane coincident with their axis of rotation, the antagonistic cable pairs remain equal in length at rest (l_{ref}). When actuating the mechanism, the directly controlled joint is referred to as the independent joint (Q), whereas dependent joints are those whose motion arises as a consequence of that independent joint actuation.

The general approach to modeling circular guide channel-induced coupling is the same for both tensile and kinematic coupling. For tensile coupling, the length of each of the dependent joint's antagonistic cables (l^+ and l^-) change symmetrically with the change in Q:

$$l^+_{tensile} = l^-_{tensile} = l_{ref} + f(Q) \tag{2}$$

For kinematic coupling, the lengths change differentially:

$$l^+_{kinematic} = l_{ref} + f(Q) \tag{3}$$

$$l^-_{kinematic} = l_{ref} + f(-Q) \tag{4}$$

As identified in [13], the geometry of the circular guide channels does not result in a linear path-length change. An analytic model of the coupling geometry was initially derived; however, at this scale of miniaturization, nonlinear effects including friction, cable stretch, and manufacturing tolerances dominated the system response, rendering the analytic model insufficient for accurate compensation. Therefore, an empirical model was created to relate dependent (wrist) and independent (elbow) joints (see Section III-D).

B. Cable Kinematics (Actuation to Joint Space)

The cable kinematics establishes the relationship between actuation space and joint space variables. The vector of actuation space variables, $\theta = [\theta_1, \theta_2, \theta_3^+, \theta_3^-, \theta_{4R}^+, \theta_{4R}^-, \theta_{4L}^+, \theta_{4L}^-]^T$, is transformed to the vector of joint space variables, $\mathbf{q} = [q_1, q_2, q_3, q_{4R}, q_{4L}]^T$, through the cable routing mechanism.

For the proximal joints (elbow), which are differentially driven, the kinematic relationships are given by:

$$q_k = \frac{r_{k,shaft}}{r_{k,joint}}\theta_k, \qquad k \in \{1,2\} \tag{5}$$

where $r_{k,shaft}$ is the shaft radius of motor k around which the cable winds, and $r_{k,joint}$ is the effective radius of the corresponding joint. For the antagonistically driven distal joints (wrist and end-effector), the cable length difference for each joint is:

$$\Delta l_{motor,n} = l_n^+ - l_n^-, \qquad n \in \{3, 4R, 4L\} \tag{6}$$

where the length changes from the actuator position are calculated as:

$$l_n^\pm = l_{n,ref}^\pm + \frac{pitch_n \cdot \theta_n^\pm}{2\pi} \tag{7}$$

where $l_{n,ref}^\pm$ are the reference cable lengths when all joint space variables are equal to zero (the rest state) and $pitch_n$ is the lead screw pitch associated with this joint. The coupling-induced cable length changes due to proximal joint motions are modeled as:

$$\begin{aligned}\Delta l_{q_k} = &[l^+(k+2, q_k) - l^-(k+2, q_k)] \\ &- [l^+(k+2, 0) - l^-(k+2, 0)], \qquad k \in \{1,2\}\end{aligned} \tag{8}$$

TABLE I
MODIFIED DENAVIT-HARTENBERG PARAMETERS FOR THE ELBOW-WRIST INSTRUMENT

Joint	$\alpha_{i-1}(^\circ)$	a_{i-1} (mm)	d_i (mm)	$\theta_i(^\circ)$
1	90	6.74	0	0
2	90	5.67	0	q_1
3	90	14.25	0	q_2
4	-90	4.48	0	q_3

where $l^{\pm}(k+2, q_k)$ represent the positive and negative cable lengths for joint $(k+2)$ as functions of joint angle q_k. The distal joint angles are then computed as:

$$q_3 = \frac{\Delta l_{q_1} - \Delta l_{motor,3}}{2r_{3,joint}} \tag{9}$$

$$q_n = \frac{\Delta l_{q_2} - \Delta l_{motor,n}}{2r_{n,joint}}, \qquad n \in \{4R, 4L\} \tag{10}$$

C. Joint Kinematics (Joint to Cartesian Space)

The forward kinematics of the instrument are formally defined using the Modified Denavit-Hartenberg (MDH) convention, which transforms the joint-space variables (q_n) into the Cartesian pose of the end effector. The instrument itself possesses a 4-DoF Pitch-Yaw-Pitch-Yaw (PYPY) serial chain, with the specific MDH parameters detailed in Table I.

For comprehensive 6-DoF control testing, the instrument is mounted to a Franka Research 3 robot, which provides two proximal degrees of freedom: prismatic translation along the main tool axis and roll about the same axis. The Franka is constrained to provide only these two DoFs, resulting in a final PRRRRR joint configuration, as detailed in Figure 1. The forward kinematic chain is computed via successive transformations using modified Denavit-Hartenberg (DH) parameters [17].

A critical distinction of this kinematic architecture emerges when comparing it to conventional non-elbowed surgical instruments. Standard instruments achieve 6-DoF control using a spherical wrist, which kinematically decouples position and orientation: the proximal joints govern the wrist center location, while the distal joints dictate the end-effector orientation [18].

Introducing proximal articulation in the elbow-wrist instrument comes at the expense of this true spherical wrist. The tool can only be modeled with a spherical wrist when both elbow joints (Q_1, Q_2) remain at their zero-degree positions. Once either elbow joint articulates, the distal wrist becomes physically offset from the primary roll axis of the main shaft. Consequently, any subsequent roll motion sweeps the tool tip along an arc rather than rotating it in place, shifting its Cartesian position.

This coupling of position and orientation necessitates a more complex control strategy than a standard spherical wrist requires. Unlike a decoupled system, a pure orientation or position change cannot be commanded by actuating distinct joint subsets. Instead, achieving a desired orientation change while maintaining the tool tip position requires the simultaneous, coordinated motion of the elbow joints during roll, thereby enabling full 3-DoF orientation control at the wrist.

D. Coupling Compensation

To counteract the kinematic relationships outlined above, a real-time compensation strategy is implemented. The algorithm actively counteracts the coupling-induced cable length changes. For a given proximal motion of $q_k, k \in \{1,2\}$, affecting distal joint n, $n \in \{3, 4R, 4L\}$, the algorithm operates as follows:

1) **Calculate Coupling Effect**: The induced cable length difference, $\Delta l_{coupling}$, is calculated as in Eq. 8.
2) **Determine Required Motor Action**: The required motor differential angle to counteract this coupling is:

$$\Delta\theta_{required} = \frac{\Delta l_{coupling} \cdot 2\pi}{p_n} \tag{11}$$

where p_n is the cable pitch for joint n. This difference is split equally between the antagonistic motor pair:

$$\Delta\theta_{comp} = \frac{\Delta\theta_{required}}{2}. \tag{12}$$

3) **Apply Real-time Compensation:** The compensating motor commands are added to the desired motor commands in the control loop:

$$\theta_n^{\pm} = \theta_n^{\pm} \pm \Delta\theta_{\text{comp}}. \tag{13}$$

This feed-forward compensation strategy ensures that distal joints remain stationary during proximal joint motions, enabling decoupled and intuitive control of the instrument.

The implementation of this control structure requires computing $\Delta l_{coupling}$ for three distinct types of coupling within the system. The spiral tensile couplings (Q1-Q2 and Q2-Q3) were mathematically evaluated and found to induce negligible path length changes, allowing them to be omitted from the compensation strategy (see Section III). The circular tensile coupling (Q3-Q4) was actively compensated using the model derived and validated in [13]. Because the analytical geometry alone was insufficient for the remaining circular kinematic couplings (Q1-Q3 and Q2-Q4), empirical testing was conducted to define these relationships. To compute $f(Q)$ for the kinematic couplings, empirical fourth-degree polynomial models were derived (detailed in Section IV-B) to relate the angular position of the dependent joint $(q_{dependent})$ to the independent joint (Q). The effective radius of the downstream link $(r_{dependent})$ was then used to translate this angular relationship into the required change in path length:

$$f(Q) = (r_{dependent}) \cdot (q_{dependent}) \tag{14}$$

IV. PERFORMANCE ANALYSIS AND EXPERIMENTAL VALIDATION

A. Workspace and Dexterity Analysis

The manipulability index is a measure of how dexterous the manipulator is at certain points in the workspace, and was derived using the Jacobian with the Yoshikawa method [19]. High manipulability values indicate that the manipulator can generate end-effector velocities effectively in multiple

directions, reflecting greater dexterity. The manipulability-based workspace analysis result is shown in Fig. 4. The lower third of the sphere-like workspace demonstrates that the proposed kinematic design maintains high distal manipulability, making it well-suited for executing complex tasks in confined and deep workspaces. This would align well with operating deeper within the oropharyngeal cavity. By decoupling the distal workspace from the sweeping shaft motions required by conventional straight-shaft instruments, the proximal elbow enables the system to maintain high manipulability values within highly constrained anatomical spaces. Tasks such as suturing and precise tissue dissection, which require sustained multi-directional force application at depth, are representative examples that would benefit from this high-manipulability region. A full sensitivity analysis quantifying tip displacement per unit joint increment is a planned extension of this work.

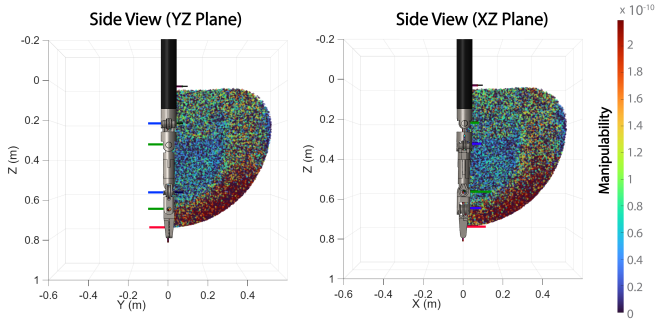

Fig. 4. Voxelized manipulability-encoded workspace. The tool is shown in its home position with the proximal base frame. Link lengths are magnified 20x for visualization. Left) YZ plane, Right) XZ plane illustrating high distal manipulability, which is optimal for performing complex tasks deep within cavities such as the oropharyngeal space.

B. Development of Empirical Compensation Model

Experimental validation sought to evaluate the feasibility of the proposed compensation strategy. First, the empirical models described in Section III-D were derived from experimental values for kinematic coupling relationships. These models were then implemented into the control system to evaluate their effectiveness in minimizing the unintended motion of the downstream wrist joints relative to the upstream elbow joints.

1) Experimental Setup and Data Collection: A stereo camera system (Teledyne FLIR LLC, Wilsonville, OR, USA) was used to capture high-resolution images of the instrument. To facilitate tracking, markers were painted on either side of the rotational axis of each joint (Q1, Q2, Q3, and Q4) and at the tool's base (Fig. 3b). Prior to data collection, the stereo cameras were calibrated using MATLAB's Stereo Camera Calibrator app. The three-dimensional (3D) position of each marker was computed from the stereo images using triangulation, providing non-contact measurement of the robot's joint positions.

To derive the empirical coupling models, systematic benchtop experiments were conducted. The tool was first initialized in a centered, straight configuration (90°). To isolate the specific in-plane coupling effects, joints not under evaluation were fixed in their neutral positions. The independent elbow joints (Q1 and Q2) were then commanded through their full range of motion while the dependent wrist joints (Q3 and Q4) received no motor commands.

Actuation was executed using the smallest consistently controllable motor movement for the current hardware iteration, which was 50 steps. Given the capstan circumference of 15.7 mm per revolution, this resulted in discrete data collection increments of approximately 7° for Q1 and 8.5° for Q2. The resulting motion of both the independent elbow joints and the dependent wrist joints was recorded using the vision system at each increment.

2) Coupling Quantification Results: The above procedure was repeated to quantify the coupling in each in-plane pair (Q1-Q3, Q2-Q4). The maximum amount of coupling resulting from moving between joint limits was 116.59° for Q1-Q3 and 119.72° for Q2-Q4. From this dataset, fourth-degree polynomial models were derived to describe the relationship between the dependent and independent joints across the full range of motion. The derived models were well fit, with R^2 values of 0.994 and 0.9877 for Q1-Q3 and Q2-Q4 coupling, respectively (Fig. 5).

C. Compensation Performance Evaluation

The derived models were implemented into the control system and the data collection protocol was repeated, recording joint angles for each coupling pair while commanding only the upstream joint. Results are presented in Fig. 6 and Table II, with the uncompensated case re-plotted as a baseline. For Q1–Q3, compensation reduced the maximum deviation from 116.59° to 17.02° and the average coupling rate from 0.82°/° to 0.14°/° (82.9% reduction). For Q2–Q4, the single-layer model yielded a residual average rate of 0.33°/°, insufficient given the lower R^2 of that model. A second compensation layer was therefore fit to the first-layer residuals, with the final $\Delta\theta_{\text{comp}}$ computed as the sum of both layers, reducing the average rate to 0.15°/° (80.8% reduction from the uncompensated baseline of 0.78°/°). Pre-calculated models were used throughout to minimize computational overhead.

It was observed that while the empirical models successfully captured the full range of motion, compensation performance was optimal near the center of the workspace and degraded slightly near the extreme joint boundaries. This degradation is attributed to increased cable-to-channel friction at extreme joint angles, where the non-linear relationship between cable path-length and joint rotation is most pronounced.

D. Integrated System Demonstration

As a final validation, the 4-DoF elbow-wrist surgical tool was integrated with the Franka robot (7-DoF), yielding an 11-DoF teleoperated platform in which the Franka supplied prismatic and roll motion of the proximal shaft using a software-defined RCM. The system demonstrated

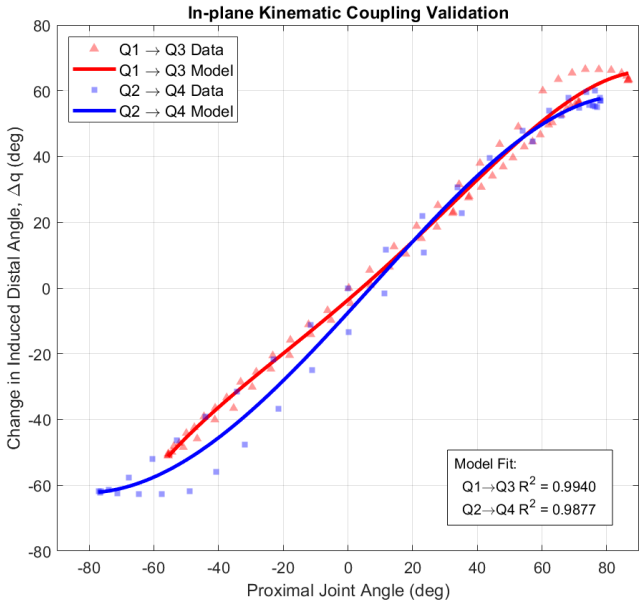

Fig. 5. Experimentally derived model of in-plane mechanical kinematic coupling used to create the empirical compensation model.

TABLE II

SUMMARY OF JOINT COUPLING PERFORMANCE METRICS

Condition	Peak-to-Peak (°)	Max. Rate (°/°)	Avg. Rate (°/°)
Q1→Q3 Uncomp.	116.59	1.07	0.82
Q1→Q3 Emp.	17.02	0.35	0.14
Q2→Q4 Uncomp.	119.72	1.09	0.78
Q2→Q4 Emp. (1-Layer)	47.85	1.04	0.33
Q2→Q4 Emp. (2-Layer)	16.16	0.67	0.15

Note: Peak-to-Peak is the worst-case induced motion over the full range; **Max. Rate** is the highest instantaneous coupling sensitivity; **Avg. Rate** is the mean instantaneous rate of change. Lower is better for all. "Uncomp." and "Emp." stand for "Uncompensated" and "Empirical", respectively.

stable and intuitive teleoperation using the kinematic model with real-time compensation, confirming the feasibility of coordinated multi-DoF control for TORS applications (Fig. 3). These results establish a critical step toward translational application, demonstrating that the proposed tool can be effectively deployed within a clinically relevant robotic framework to support dexterity-intensive procedures such as pediatric TORS. A supplementary video highlights the enhanced dexterity and range of motion achieved in this integrated configuration.

V. DISCUSSION

This study presents a novel elbow-wrist mechanism optimized for the oropharyngeal workspace, enabling high distal dexterity and manipulability for TORS procedures in a miniaturized package. Integrating a 4-mm elbow with a 3-mm wrist, this tool represents the smallest fully articulated rigid-link TORS instrument. The novel "sandwich" link architecture minimizes component count and successfully enables the high-density routing of eight tendons required for 6-DoF motion. Furthermore, the instrument relies on a

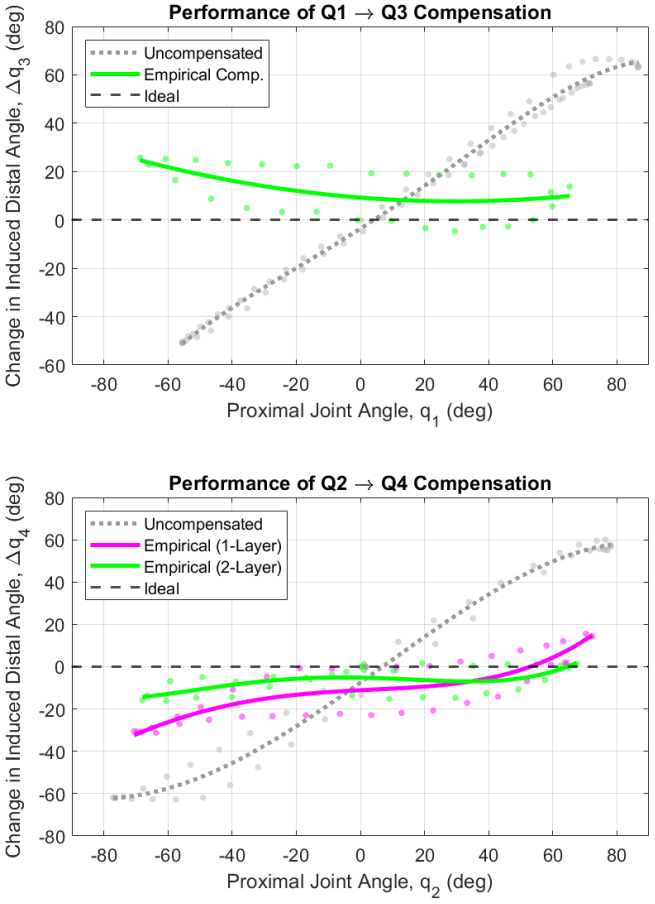

Fig. 6. Experimental results of the empirical compensation method. Top: Q1-Q3 compensation, Bottom: Q2-Q4 compensation. Black dotted line: the ideal fully decoupled relationship between joints. Grey line: recorded coupling in the uncompensated system. Purple line (Q2-Q4 only): First layer empirical compensation. Green line: empirical compensation (Q1-Q3), second layer empirical compensation (Q2-Q4).

rigid-link architecture machined from stainless steel rather than flexible continuum mechanisms, ensuring high structural rigidity during tissue interaction.

Existing mechanisms with a distal elbow are primarily intended for single-port systems [10], [20], using the elbow to create separation between instruments once within a body cavity rather than to navigate narrow anatomical corridors. While a 5-mm handheld continuum elbow-wrist tool was previously developed [21], our 3-mm/4-mm pin-jointed design offers significantly more compact articulation, improving manipulability within highly constrained spaces like the pediatric oropharynx.

Experimental results demonstrated kinematic coupling (Fig. 5). However, our empirical compensation strategy effectively mitigated these effects, reducing the average coupling rate by 82.9% for Q1–Q3 and 80.8% for Q2–Q4. These results also demonstrated the capability of this control system to progressively improve coupling mitigation with further layers of compensation. Future control optimization could integrate an analytic kinematic model; however, addressing non-linear effects at this micro-scale—such as friction, hysteresis, and cable backlash—will necessitate closed-loop or

data-driven approaches. Methods such as Gaussian Mixture Models [22], visual servoing [23], or adaptive control [24], [25] have successfully improved precision in similar non-linear microsurgical robotic applications.

Integration of the novel tool with a Franka manipulator establishes a platform for comprehensive system-level evaluation. By modifying the macro-manipulator's prismatic constraints, the system can mimic other surgical platforms like the dVRK. Future characterization will quantify the tool's load capacity, force transmission, and actuation speed, alongside evaluating its capability to perform dexterity-intensive tasks within high-fidelity simulated environments to guide subsequent in-vivo validation.

VI. Conclusion and Future Work

This study presents a novel 6-DoF elbow-wrist instrument at 3-mm in diameter, representing the first demonstration of a fully articulated elbow-wrist mechanism at this scale for TORS. The novel link architecture enables high-density cable routing within a 4-mm elbow profile, providing the mechanical hardware foundation necessary for dexterous access to confined surgical workspaces such as the pediatric oropharyngeal cavity. An empirical multi-layer compensation strategy achieved greater than 80% reduction in kinematic coupling, enabling decoupled joint control. Integration with a Franka Research 3 manipulator demonstrated coordinated macro-micro teleoperation of the combined system. Future work will evaluate performance of dexterity-intensive surgical tasks—such as suturing and tissue dissection—in high-fidelity simulated environments prior to in-vivo validation. Future characterization should also address load capacity, structural stability under applied forces, and actuation speed, which are important performance metrics for clinical translation that were beyond the scope of this initial demonstration.

References

[1] J. R. Oliver *et al.*, "Transoral robotic surgery adoption and safety in treatment of oropharyngeal cancers," *Cancer*, vol. 128, no. 4, pp. 685–696, Nov. 2021.

[2] K. Gangwani, L. Shetty, R. Seshagiri, and D. Kulkarni, "Comparison of tors with conventional surgery for oropharyngeal carcinomas in t1–t4 lesions," *Annals of Maxillofacial Surgery*, vol. 9, no. 2, p. 387, Jan. 2019.

[3] T. F. Krebs, J.-H. Egberts, U. Lorenzen, M. F. Krause, K. Reischig, R. Meiksans, J. Baastrup, A. Meinzer, I. Alkatout, G. Cohrs, H. Wieker, A. Lüthje, S. Vieten, G. Schultheiss, and R. Bergholz, "Robotic infant surgery with 3 mm instruments: a study in piglets of less than 10 kg body weight," *Journal of Robotic Surgery*, vol. 16, no. 1, pp. 215–228, Feb. 2022.

[4] D. R. Johnston, S. E. Maurrasse, and J. M. Maddalozzo, "Avascular midline oropharyngeal anatomy allows for expanded indications for transoral robotic surgery in pediatric patients," *Journal of Robotic Surgery*, vol. 17, no. 4, pp. 1803–1808, Apr. 2023.

[5] S. Roy and B. Smith, "Robotic surgery in pediatric otolaryngology," *International Journal of Head and Neck Surgery*, vol. 7, no. 2, pp. 120–123, Jan. 2016.

[6] J. Meulemans, "Transoral robotic surgery (tors) using the da vinci xi: prospective analysis of feasibility, safety, and outcomes," *Head & Neck*, vol. 44, no. 1, pp. 143–157, 2021.

[7] K. N. Rao and K. K. Gangiti, "Transoral robotic surgery," *Indian Journal of Surgical Oncology*, vol. 12, no. 4, p. 847–853, 2021.

[8] M. Hagen and M. Curet, "The da vinci surgical® systems," in *Robotic Surgery*. Springer, 2014, pp. 9–19.

[9] da Vinci Research Kit Consortium, *User Guide for the da Vinci Research Kit (dVRK)*, Johns Hopkins University and collaborators, Jan. 2019, version: Jan 2019. [Online]. Available: https://github.com/jhu-dvrk/sawIntuitiveResearchKit/releases/download/1.6.0/User_Guide_DVRK_Jan_2019.pdf

[10] Intuitive Surgical, Inc., "Da vinci SP," https://www.intuitive.com/en-us/products-and-services/da-vinci/sp, Intuitive Surgical, Inc.

[11] A. Costantino, C. Sampieri, P. G. Meliante, A. D. Virgilio, and S.-H. Kim, "Transoral robotic surgery in oropharyngeal squamous cell carcinoma: A comparative study between da vinci single-port and da vinci xi systems," *Oral Oncology*, vol. 148, p. 106629, Jan. 2024.

[12] C. Sampieri *et al.*, "Single-port versus multiport da vinci system for transoral robotic surgery of hypopharyngeal and laryngeal carcinoma," *Otolaryngology*, vol. 169, no. 3, pp. 548–555, Feb. 2023.

[13] G. C. Wu, D. J. Podolsky, T. Looi, L. A. Kahrs, J. M. Drake, and C. R. Forrest, "A 3 mm wristed instrument for the da vinci robot: Setup, characterization, and phantom tests for cleft palate repair," *IEEE Transactions on Medical Robotics and Bionics*, vol. 2, no. 2, pp. 130–139, 2020.

[14] D. J. Podolsky, E. Diller, D. M. Fisher, K. W. Wong Riff, T. Looi, J. M. Drake, and C. R. Forrest, "Utilization of cable guide channels for compact articulation within a dexterous three degrees-of-freedom surgical wrist design," *Journal of Medical Devices*, vol. 13, no. 1, p. 011003, 2019.

[15] G. Maguire, E. Tang, T. Looi, and D. Podolsky, "Robotic assisted cleft palate repair using novel 3 mm tools: A reachability and collision analysis," *IEEE Transactions on Biomedical Engineering*, vol. 72, no. 7, pp. 2085–2094, 2025.

[16] C. Ho, T. Looi, G. Maguire, and D. J. Podolsky, "Characterization of friction within a novel 3 mm wristed robotic instrument," in *Actuators*, vol. 13, no. 9. MDPI, 2024, p. 326.

[17] J. J. Craig, *Introduction to Robotics: Mechanics & Control*, 4th ed. Boston, MA: Pearson, 2017.

[18] M. Brandstötter, A. Angerer, and M. Hofbaur, "An analytical solution of the inverse kinematics problem of industrial serial manipulators with an ortho-parallel basis and a spherical wrist," *ResearchGate*, May 2014, accessed: Sep. 14, 2025. [Online]. Available: https://www.researchgate.net/publication/264212870_An_Analytical_Solution_of_the_Inverse_Kinematics_Problem_of_Industrial_Serial_Manipulators_with_an_Ortho-parallel_Basis_and_a_Spherical_Wrist

[19] T. Yoshikawa, "Analysis and control of robot manipulators with redundancy," in *Preprints of 1st Int. Symp. of Robotics Research, Boston, MA, 1983*, 1983, pp. 735–747.

[20] Vicarious Surgical. (2024, Jan.) Vicarious surgical — surgical robotics technology. Accessed: Sep. 14, 2025. [Online]. Available: https://www.vicarioussurgical.com/

[21] K. E. Riojas, P. L. Anderson, R. A. Lathrop, S. D. Herrell, D. C. Rucker, and R. J. Webster, "A hand-held non-robotic surgical tool with a wrist and an elbow," *IEEE Transactions on Biomedical Engineering*, vol. 66, no. 11, pp. 3176–3184, Feb. 2019.

[22] M. Esfandiari, Y. Zhou, S. Dehghani, M. Hadi, A. Munawar, H. Phalen, D. E. Usevitch, P. Gehlbach, and I. Iordachita, "A data-driven model with hysteresis compensation for i2ris robot," in *2024 International Symposium on Medical Robotics (ISMR)*, 2024, pp. 1–7.

[23] M. Azizian, M. Khoshnam, N. Najmaei, and R. V. Patel, "Visual servoing in medical robotics: A survey. part i: Endoscopic and direct vision imaging – techniques and applications," *International Journal of Medical Robotics and Computer Assisted Surgery*, vol. 10, no. 3, pp. 263–274, Sept. 2013.

[24] J. Hong, D. Hong, C. Kim, and S. Won, "Adaptive hybrid control for backlash-like hysteresis and marker-based pose estimation in endoscopic robots," *IEEE Robotics and Automation Letters*, vol. 10, no. 7, pp. 7015–7022, 2025.

[25] Z. Wang, T. Wang, B. Zhao, Y. He, Y. Hu, B. Li, P. Zhang, and M. Q.-H. Meng, "Hybrid adaptive control strategy for continuum surgical robot under external load," *IEEE Robotics and Automation Letters*, vol. 6, no. 2, pp. 1407–1414, 2021.